Supporting Information

for

Defect-engineered graphitic carbon nitride on carbon cloth supports for the photoelectrocatalytic degradation of organophosphate pesticides

Giacomo Marchiori,[a] Roberta Seraglia,[b] Gian Andrea Rizzi,[a,b] Chiara Maccato,[a,b]*

Mattia Benedet,[a,b] Emanuela Callone,[c] Sandra Dirè,[c] Alberto Gasparotto,[a,b] and Davide Barreca[b]

[a] Department of Chemical Sciences, Padova University and INSTM, Via Marzolo, 1 - 35131 Padova, Italy.

[b] CNR-ICMATE and INSTM, Department of Chemical Sciences, Padova University, Via Marzolo, 1, and Corso Stati Uniti, 4 - 35131 Padova, Italy.

[c] "*Klaus Müller*" Magnetic Resonance Laboratory, Department of Industrial Engineering – Trento University, Via Sommarive, 9 - 38123 Trento, Italy.

* Corresponding author. E-mail: chiara.maccato@unipd.it .

§ S1. Synthesis of gCN powders and deposition on carbon cloths

Synthesis of gCN (U): 6.00 g of urea (Thermo Scientific, ≥ 98 %), finely pre-grinded, were placed in a covered ceramic crucible and heat-treated in a muffle furnace in air (550°C, 2 h), followed by slow cooling at room temperature.

Synthesis of gCN (U+AcAc): 6.00 g of urea, finely grinded in a mortar, were suspended in 25 mL of isopropyl alcohol, along with 0.5 mL of acetylacetone (AcAc; Alfa Aesar, 99 %). The used molar ratio of AcAc to urea (0.05) has been optimized in a previous study.[1] After sonication for 30 min, isopropyl alcohol was allowed to slowly evaporate, and the obtained powders were annealed under the above reported conditions.

gCN deposition on carbon cloths: The procedure, re-adapted from literature, has already been successfully employed and optimized by our groups in previous works.[2, 3] As reported in main paper (see caption to Scheme 1), the suspensions employed for EPD were obtained by mixing acetone, I_2 and nitride powers [either gCN (U) or gCN (U+AcAc)]. Upon dissolution in acetone, I_2 reacts with the solvent, by means of α-halogenation, generating H^+ ions which are easily adsorbed on gCN flakes, due to the presence of uncondensed electron-rich -NH_x surface groups. Thus, the positively charged carbon nitride can be deposited onto the carbon cloth, by applying to the latter a negative bias, without the necessity of using any electrolyte to increase the suspension's conductivity.

Depositions were performed on carbon cloths (CC; Quintech, E35; lateral dimensions = 2 cm × 1 cm), pre-cleaned by sequential sonication in deionized water, isopropanol, and acetone (10 min for each). During each deposition, a digital multimeter (Agilent 34405A) was used to apply the potential between the CC substrate and a graphite counter-electrode (distance fixed at 20 mm). Operating EPD conditions [10 V, 30 s for gCN (U); 10 V, 45 s for gCN (U+AcAc)] were optimized through a series of preliminary experiments, in order to deposit the same material amount in the two cases (≈ 0.40 mg). After EPD, all samples underwent an annealing treatment in air (400°C, 2 h), followed by slow cooling at room temperature.

§ S2. Characterization

Solid state nuclear magnetic resonance (NMR) analyses were carried out with a Bruker Avance 400WB spectrometer. NMR spectra were acquired with both cross polarization and single pulse sequences under the following conditions: ^{13}C frequency: 100.48 MHz, π/2 pulse 4.4 μs, cp pulse 3 ms, decoupling length 5.9 μs, recycle delay: 10 s, 10k scans; for single pulse 40 s recycle delay, 100 scans. ^{15}N frequency: 40.55 MHz, cp pulse 5 ms, decoupling length 5.9 μs, recycle delay: 10 s, 24k scans. ^{1}H frequency: 400.13 MHz, π/2 pulse 5 μs, recycle delay 5 ms, 16 scans. Samples were packed in 4 mm zirconia rotors and spun at 8 kHz under air flow. Adamantane CH_2 at 38.48 ppm and glycine NH_2 at 34 ppm were used as external secondary references.

During both electrochemical and electro-Fenton (EF) experiments, the circuit was controlled by an Autolab workstation (PGSTAT204 potentiostat/galvanostat). For photoactivated tests, the working electrode was exposed to a white light LED lamp Philips LUMILEDS LXML-PWN1 0120 (intensity ≈150 mW/cm^2), placed at a distance of 10 cm from the cell centre (Fig. S1). Before each electrochemical test, the solution was saturated with O_2 and its pH was adjusted to 3.00 by a controlled addition of 1 M H_2SO_4, in order to operate under optimized electro-Fenton conditions.[4]

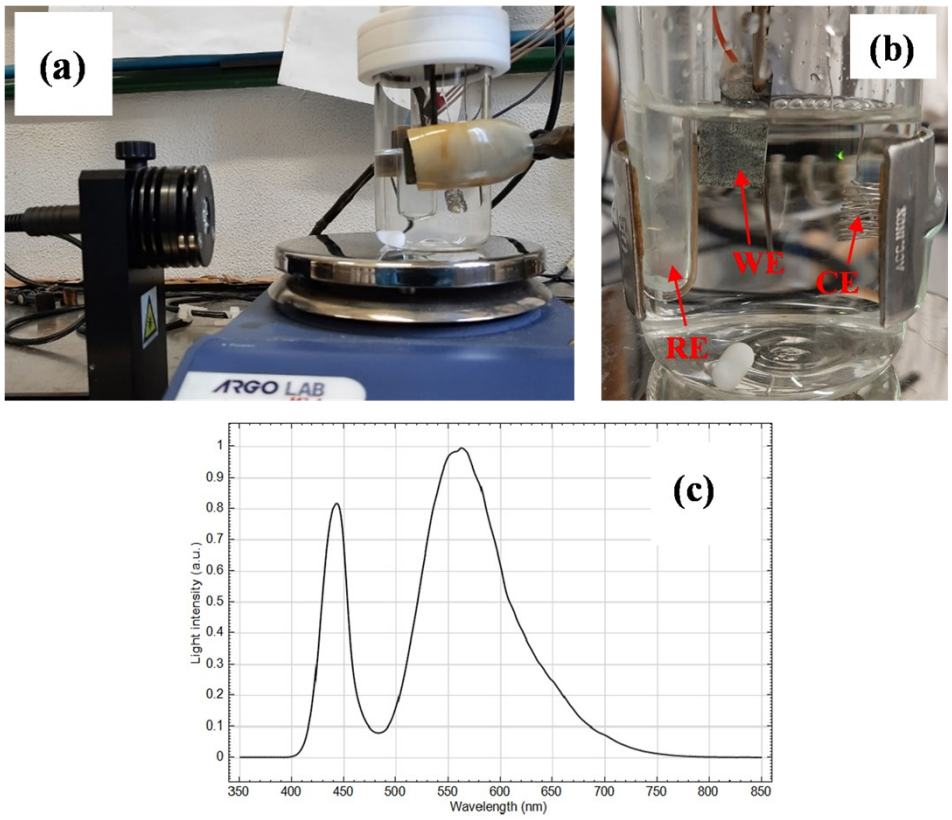

Figure S1. (a) Instrumental setup used for electrochemical characterization. (b) Frontal close-up of the assembled cell (RE: reference electrode, WE: working electrode, CE: counter electrode). (c) Emission spectrum of the LED lamp Philips LUMILEDS LXML-PWN1 0120, used in the present work.

For electrochemical analyses, the target materials were used as working electrodes, whereas a saturated calomel electrode (SCE, E_{SCE}) and a Pt coil were employed as reference and counter electrode, respectively. All the recorded electrochemical data were converted from the SCE into the reversible hydrogen electrode (RHE) scale, using the equation:

$$E_{RHE}(V) = E_{WE}(V) + E_{SCE}(V) + 0.0592 \times pH \qquad (S1)$$

where E_{WE} indicates the bias applied to the working electrode.

Cyclic voltammetries (CV) were performed in a potential range between +1.75 and -0.65 V *vs.* RHE (scan rate = 0.025 V/s). Linear sweep voltammetries (LSV), both in the dark and under illumination, were collected in the same bias interval, from positive to negative potentials (scan rate = 0.010 V/s). Chronoamperometry (CA) traces were acquired keeping the solution under constant stirring and

bubbling O_2 inside it. The voltage applied to the working electrode (+0.06 V *vs.* RHE) corresponded to the potential of maximum reduction of O_2 toH_2O_2, as indicated by LSV measurements (see Fig. 4b-c, main paper).

EF tests for Fenitrothion (FNT) degradation were carried out in the same cell and with the same three-electrode configuration employed for the electrochemical characterization. Experiments were performed at pH = 3.00, as already stated.[4] Before each test, a series of fifteen activation CVs were applied to the working electrode (scan rate = 0.1 V/s; potential range = +1.75 ÷ -0.65 V *vs*. RHE), to preliminarily probe the sample stability and clean their surface from any incidentally adsorbed impurity. Subsequently, 10 mg of $FeSO_4 \cdot 7H_2O$ (Sigma Aldrich, 99 %) were dissolved into the solution, providing a nominal Fe^{2+} concentration of 0.51 mM.[4] Degradation tests were started illuminating the sample, while bubbling O_2 inside a 0.1 M Na_2SO_4 "mother" aqueous solution containing 30 ppm (μg/L) of FNT (Sigma Aldrich, ≥ 95%), under constant stirring. In each degradation test, 70 mL of FNT-containing solution were used, and a fixed potential of +0.06 V *vs.* RHE was set to the working electrode. Once prepared, the FNT solution was stored in the dark, and all tests were conducted within one week after its preparation.

During each test, six different fractions were taken from the solution at 0, 1, 2, 4, 6, and 24 h, starting from the bias and illumination application, for high performance liquid chromatography-mass spectroscopy (HPLC-MS) analyses, to monitor FNT degradation. All the collected samples were promptly stored in sealed vials, kept at ≈ 4°C and protected from light prior analysis.

After the conclusion of EF experiments, the pH of the solution was found to be comprised between 2.85 and 2.90, irrespective of the employed working electrode.

With the aim of making a thorough comparison, a "blank" degradation test was also performed, placing the FNT solution inside the cell, acidifying it to pH = 3.00 and irradiating the cell for 24 h, without the electrodes and, therefore, without the application of any external voltage.

HPLC-MS experiments were performed with a LCQFleet ion trap instrument (ThermoFisher Scientific), operating in positive and negative ion modes, coupled with a Surveyor LC Pump Plus (ThermoFisher Scientific) and with a UV-Vis detector Accela PDA Detector (ThermoFisher Scientific). The used entrance capillary temperature and voltage were set at 275°C and ±4 kV, respectively. The ion source temperature was maintained at 300°C. The used N_2 flows were set as: sheath gas: 25 a.u.; auxiliary gas: 10 a.u.; sweep gas: 5 a.u.

MS^n experiments were performed by applying a supplementary radio frequency voltage to the end caps of the ion trap (5 V peak-to-peak).

Samples were injected (25 μL) into a Luna^R Omega 5 mm C18 100 Å (250 × 4.60 mm), (Phenomenex) column. The mobile phase consisted of solvent A (0.1 % formic acid in water) and B (0.1 % formic acid in acetonitrile). The eluent composition, at a flow rate of 1 mL/min, was varied as follows: 10% B for the first 5 min; linearly increased from 10% B to 50% B for the subsequent 15 min, and afterward maintained constant for 10 min; linearly increased from 50% B to 80% B in the next 10 min, and then rapidly decreased to 10% B in the subsequent 5 min; kept constant at 10 B% for the last 5 minutes.

The mass spectrometer worked in negative ion mode from 0 to 22.50 min, and in positive ion mode from 22.50 to 50 min.

The disappearance of FNT molecule from the solution since the beginning (t = 0 h) of each EF experiment (see Fig. 6a-b, main paper, and Fig S10) prevented the employment of the HPLC-MS apparatus to quantify its concentration *vs*. time, and to reliably evaluate the amount of pesticide remaining in solution at the end of degradation tests.

Experiments in coumarin solutions were carried out on a solution containing 0.1 M Na_2SO_4 and 1.0 mM coumarin (Sigma-Aldrich, ≥ 99 %). Freshly prepared CC_U and CC_U+AcAc specimens were used as working electrode within the same setup and under the same operating conditions adopted for FNT degradation experiments. Every test lasted 6 h, and, in each case, three different fractions were

taken from the working solutions at 0, 3, and 6 h starting from the application of both bias and illumination. Fluorescence spectra of the collected fractions were subsequently recorded on a FLS1000 (Edinburgh Instruments) spectrophotometer (spectral bandwidth = 1 nm).

§ S3. Chemico-physical characterization of gCN powders

S3.1. FT-IR spectroscopy

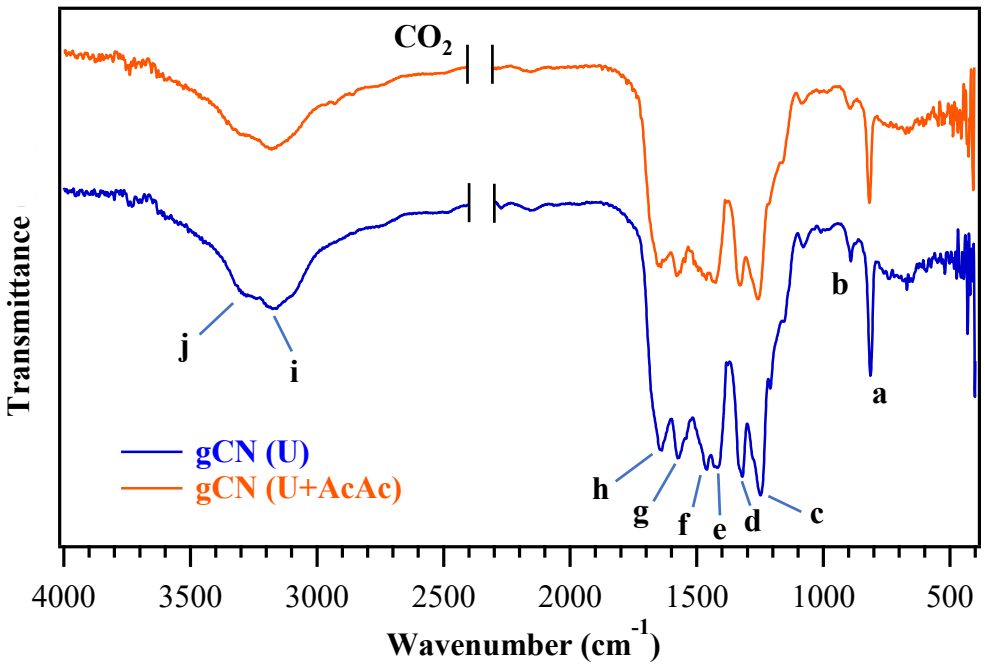

Figure S2. FT-IR spectra, recorded in diffuse reflectance mode, for gCN (U) and gCN (U+AcAc) powders. The plotted spectra have been vertically shifted for clarity.

Peak	Wavenumber (cm^{-1})	Attribution
a	814	Bending out of plane of heptazine units[5, 6]
b	891	N-H bond deformation[7]
c	1248	Stretching modes of bridging C-N(-C)-C and C-NH-C moieties between heptazine units[8]
d	1320	
e	1420	Stretching modes of C-N bonds inside heptazine units[6, 8]
f	1460	
g	1573	
h	1639	Bending modes of NH_2 groups conjugated to heptazine units[9]
i	3166	Stretching modes of N-H bonds in primary and secondary amino groups, involved in H-bonds[8, 10]
j	3293	

Table S1. Assignment of the signals observed in the FT-IR spectra of Fig. S2.

The recorded IR spectra (Fig. S2) evidenced a good agreement with the available literature data (see also Table S1).[11-14] In particular, the signal at ≈ 814 cm^{-1} and the peaks between 1200 and 1650 cm^{-1} are typical of the carbon nitride skeleton. In addition, the presence of the signal at ≈1639 cm^{-1} and the broad band around ≈3200 cm^{-1} in both powders can be attributed to the occurrence of primary or secondary amino-groups, that should not be present in an ideal gCN structure, indicating thus an incomplete condensation process[9, 15] [see also X-ray photoelectron spectroscopy (XPS) results]. The band at 3200 cm^{-1} also results from the stretching of -OH groups deriving from water molecules chemisorbed on gCN[9] (see also XPS data) or, in the case of gCN (U+AcAc), from AcAc functionalization.[16]

S3.2. Multinuclear solid state NMR analysis

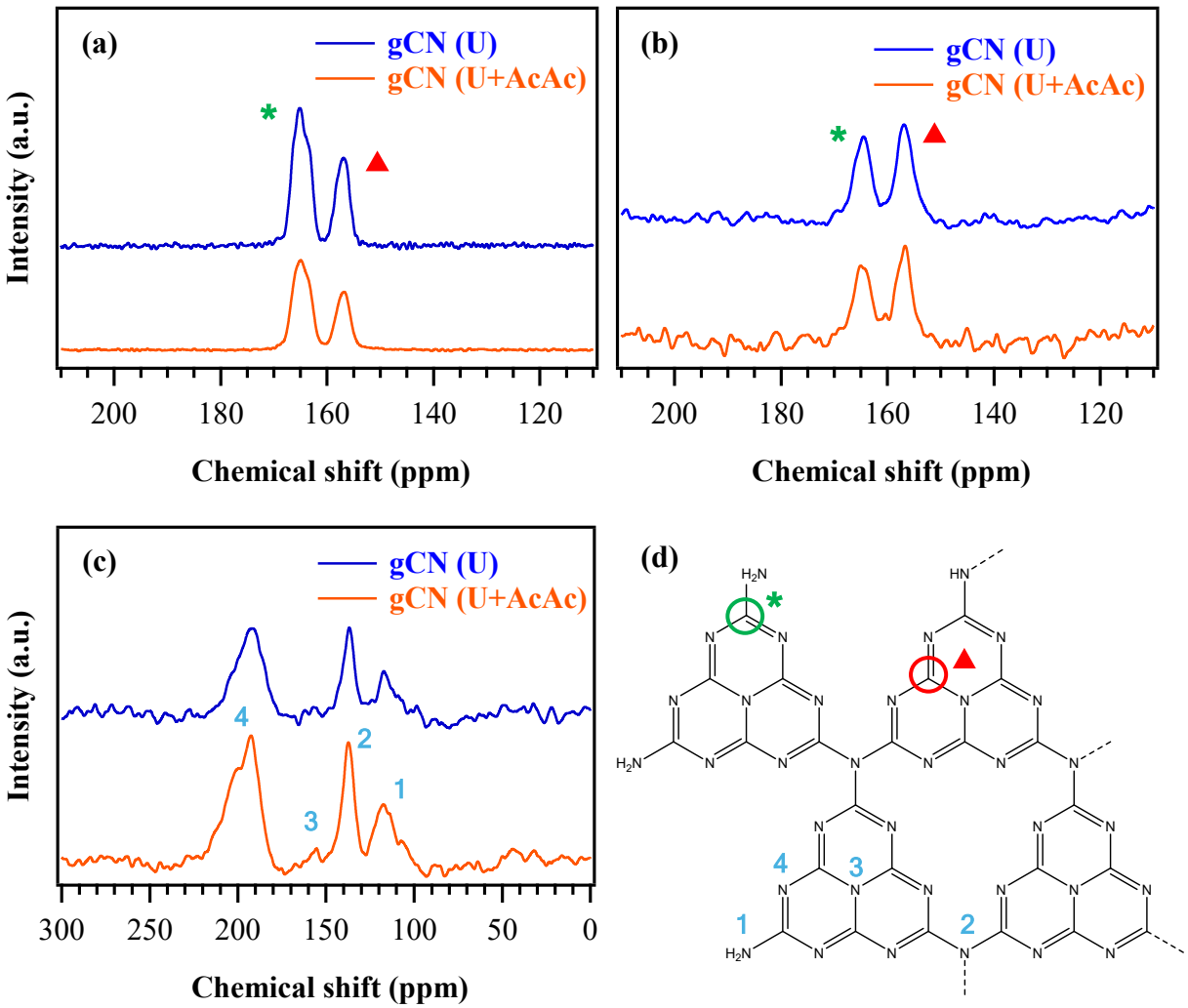

Figure S3. ^{13}C CPMAS NMR (a) and ^{13}C MAS NMR (b) spectra. ^{15}N CPMAS NMR spectra (c). gCN planar structure with signals' attribution (d).

The ^{13}C cross polarization/magic angle spinning (CPMAS) NMR spectra for both samples (Fig. S3a) are characterized by the presence of two resonances at 165 and 157 ppm. The related MAS spectra display the same two resonances, with almost equal intensity (Fig. S3b). In a ^{13}C CP spectrum the signal intensity varies due to different proximities to ^{1}H species, as ^{13}C spin polarization is transferred via $^{1}H-^{13}C$ dipolar coupling; thus, the comparison between CPMAS and MAS spectra indicates that the resonance at 165 ppm refers to C closer to H than the 157 ppm one. These observations lead, at first, to discard the presence of melamine, which is characterized by a single resonance[17, 18] in favour

of melon (tris-*s*-triazine) subunits in a gCN polymer, where the two major carbon species are in equimolar ratio.[19]

According to the literature,[20] the signal at 165 ppm can be assigned to N_2C-NH_x, *i.e.* C closer to protons of the non-polymerized NH_2 or partially polymerized NH groups, whereas the high-field resonance to N=C-N, *i.e.* internal C (Figure S3b). Moreover, the resonance at 165 ppm has an asymmetric lineshape that suggests the concurrence of two components at δ 165 and 163 ppm, respectively attributable to C-NH_2 and C-NH-C.[19] Interestingly, the lineshape of this resonance is different in the two samples, suggesting a different distribution of these structural units. The results of profile fitting analysis of ^{13}C CPMAS spectra are shown in Table S2, and indicate a slight increase of C-NH-C defects at the expenses of C-NH_2 ones in gCN (U+AcAc).

δ (ppm)	**165.5 / relative area**	**163.5 / relative area**	**157.1 / relative area**
gCN (U)	54 %	15 %	31 %
gCN (U+AcAc)	47 %	21 %	32 %

Table S2. Semi-quantitative analysis from the profile fitting of ^{13}C CPMAS NMR spectra.

Fig. S3c shows the ^{15}N spectra of the two samples. The low signal-to-noise (S/N) ratio in these NMR spectra is due to the low amount of ^{15}N isotope, the lack of coupling of some nitrogen atoms with proton-rich environments, and some degree of structural disorder. Nevertheless, up to four resonances can be identified, centred at ≈ 195, 157, 136 and 117 ppm, and attributable to C-N=C, N-C_3, -NH- and –NH_2 groups,[19, 21] respectively. These resonances display small lineshape differences in agreement with ^{13}C and the other spectroscopic data. The proposed assignment fits well with a melon structure, as already stated.[19, 21]

It is worth mentioning that NMR experiments were carried out on samples with C and N in natural abundance, which explains the low S/N ratio compared with some results in the literature and prevents a more thorough structural investigation.

§ S4. Chemico-physical characterization of supported materials

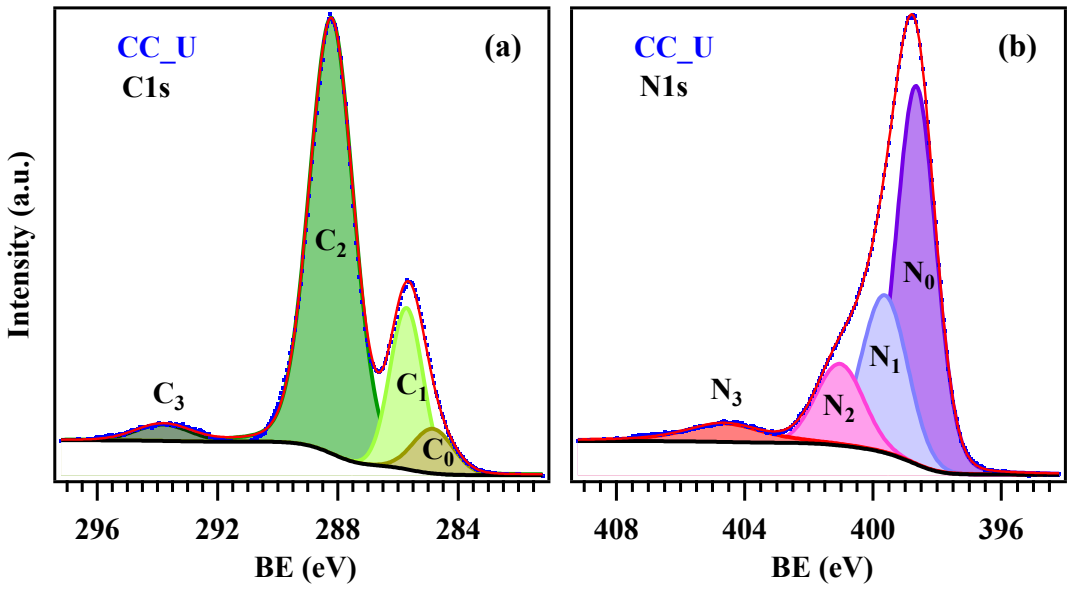

Figure S4. C1s (a) and N1s photoelectron peaks (b) of CC_U sample.

	C_0		C_1		C_2		C_3	
sample	**BE (eV)**	**%**	**BE (eV)**	**%**	**BE (eV)**	**%**	**BE (eV)**	**%**
CC_U	284.8	6.3	285.7	18.6	288.2	72.0	293.8	3.1
CC_U+AcAc	284.8	6.5	285.7	25.7	288.3	65.3	293.8	2.5

Table S3. Binding energy (BE) values and percentage contribution of the various components to the overall C1s signal for the investigated specimens. Peak labelling as in Fig. S4a and in Fig. 2b (main paper).

	N_0		N_1		N_2		N_3	
Sample	**BE (eV)**	**%**	**BE (eV)**	**%**	**BE (eV)**	**%**	**BE (eV)**	**%**
CC_U	398.7	55.7	399.6	25.3	401.0	13.7	404.8	5.3
CC_U+AcAc	398.9	53.4	399.7	24.1	401.1	17.1	404.9	5.4

Table S4. BE values and percentage contribution of the various components to the overall N1s signal for the investigated specimens. Peak labelling as in Fig. S4b and in Fig. 2c (main paper).

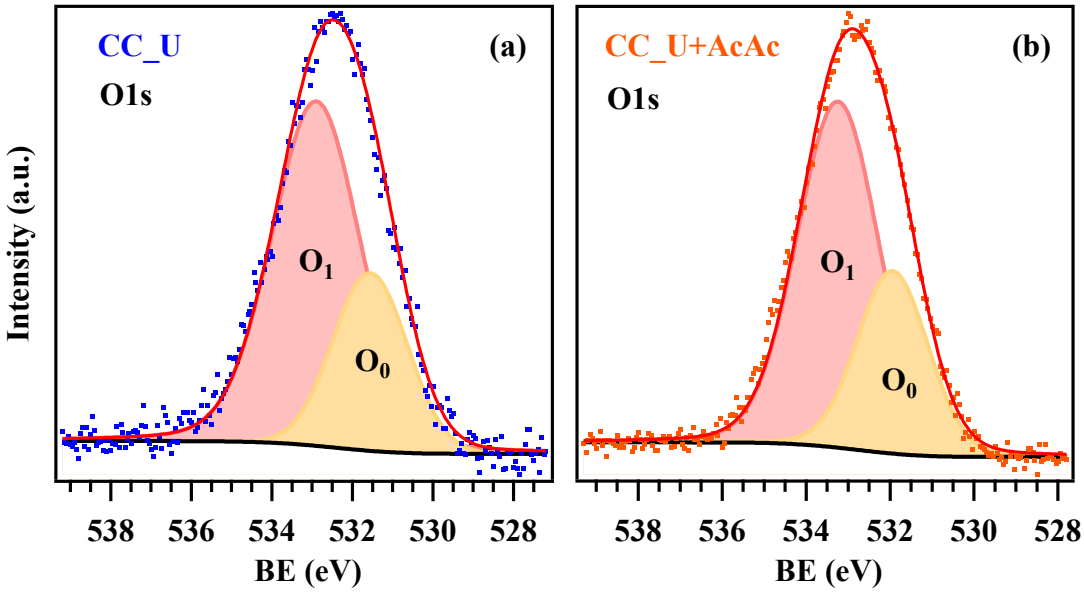

Figure S5. O1s photoelectron peaks for CC_U (a) and CC_U+AcAc (b).

	O_0		O_1	
sample	**BE (eV)**	**%**	**BE (eV)**	**%**
CC_U	531.7	28.6	533.0	71.4
CC_U+AcAc	531.8	31.0	533.2	69.0

Table S5. BE values and percentage contribution of the various components to the overall O1s signal for the investigated specimens. Peak labelling as in Fig. S5.

O1s signal fitting was carried out by two components (Fig. S5 and Table S5): **O_0**, attributable to the presence of -OH groups chemisorbed on gCN[1, 22, 23] and C-O moieties [24, 25]; **O_1** due to molecularly adsorbed water.[26-28]

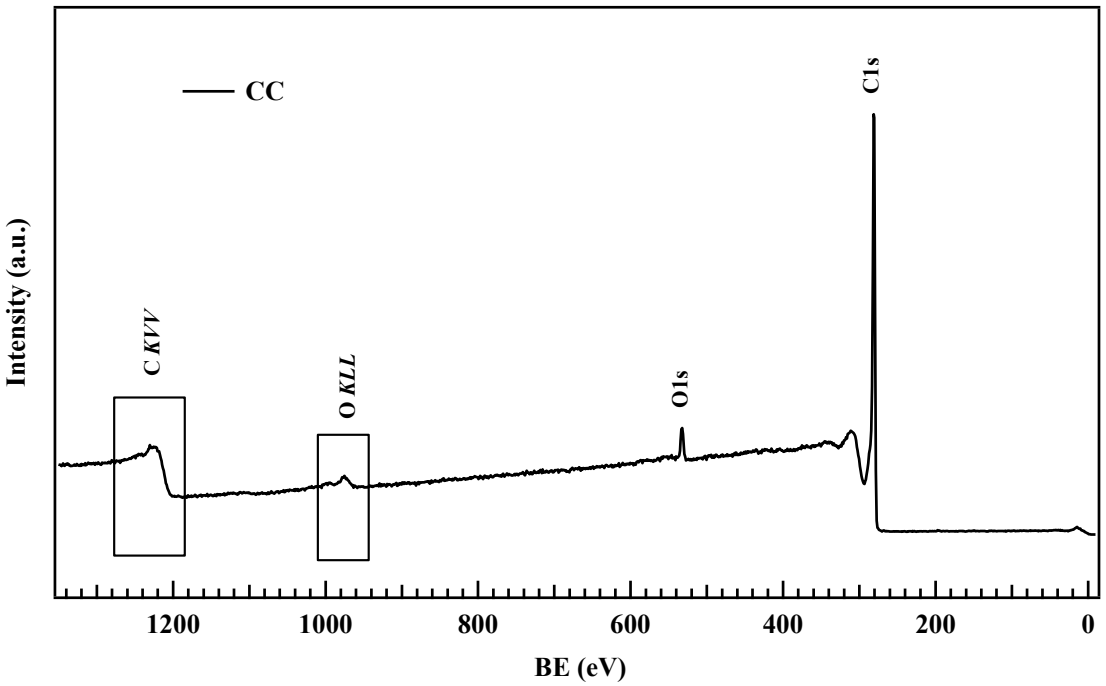

Figure S6. XPS wide-scan spectrum (survey) for the bare carbon cloth (CC).

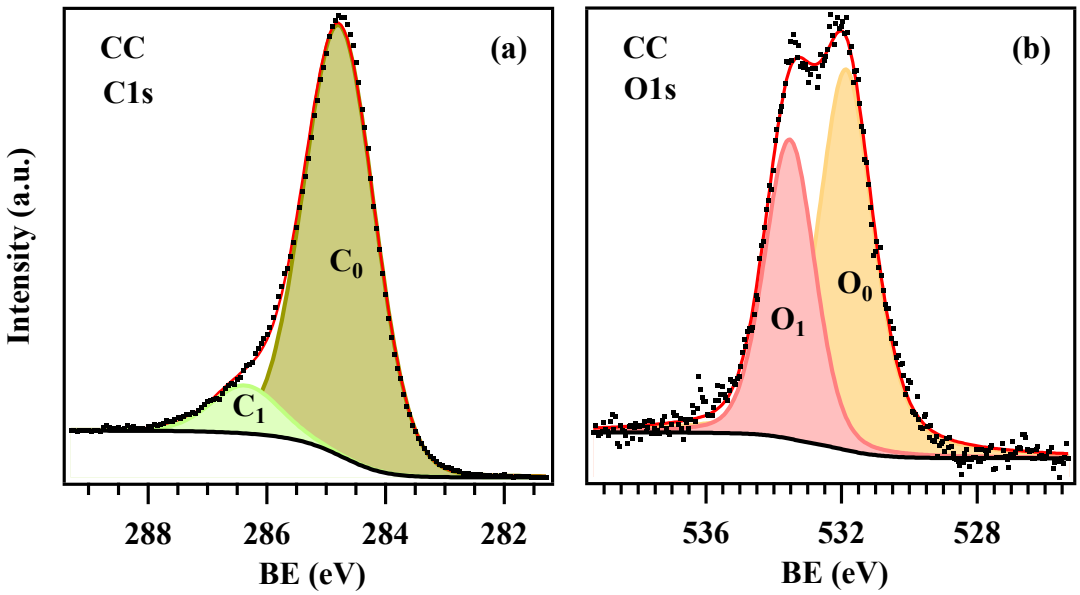

Figure S7. C1s (a) and O1s photoelectron peaks (b) of bare CC.

For the C1s photopeak (Fig. S7a), the main component $\mathbf{C_0}$ is attributable to graphitic carbon from the substrate (C-C) and adventitious contamination.[26-28] $\mathbf{C_1}$ is associated with the presence of C-O-C and C-OH groups,[26, 28] due to the surface oxidation of the material caused by exposure to air and moisture. As for O1s signal (Fig. S7b), the $\mathbf{O_0}$ component of the O1s peak is attributed to hydroxyl groups (OH)[26, 29], whereas $\mathbf{O_1}$ includes contributions from molecularly adsorbed water.[26, 27]

	C_0		C_1		O_0		O_1	
sample	**BE (eV)**	**%**	**BE (eV)**	**%**	**BE (eV)**	**%**	**BE (eV)**	**%**
CC	284.8	90.1	286.3	9.9	531.6	60.9	533.2	39.1

Table S6. BE values and percentage contribution of the various components to the overall C1s and O1s signals for the bare carbon cloth.

§ S5. Functional tests

S5.1. Cyclic voltammetry (CV)

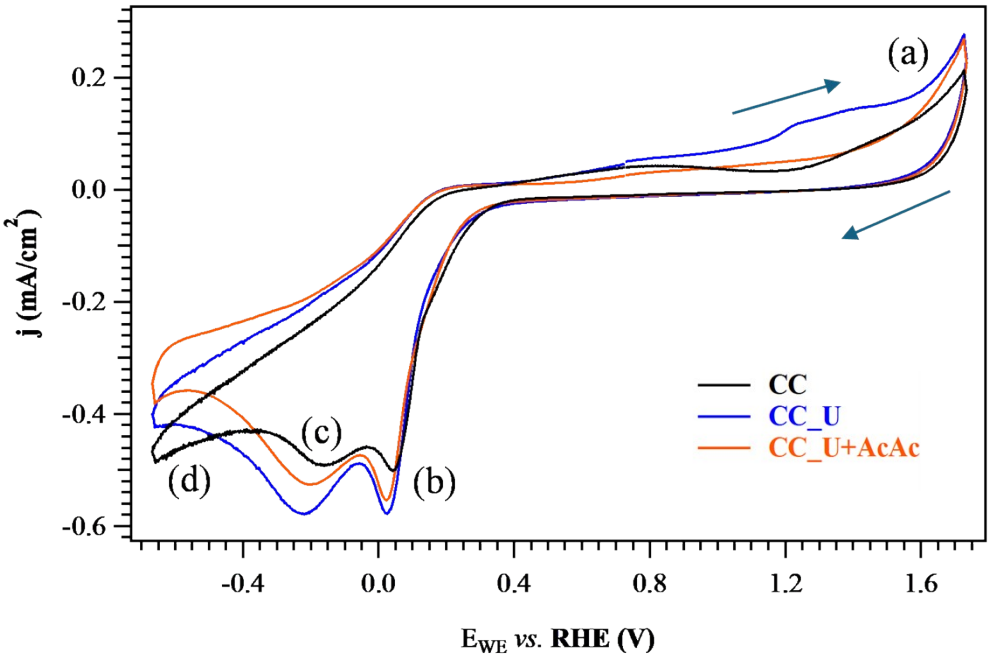

Figure S8. Cyclic voltammetries for bare CC, CC_U and CC_U+AcAc. The arrows mark the scanning direction.

All three samples present the same signals: (a) O_2 evolution from H_2O oxidation; (b) $2e^-$ ORR (oxygen reduction reaction); (c) $4e^-$ ORR; (d) H_2 evolution from water reduction.[4, 30-32]

$2e^-$ ORR constitutes the target reaction to achieve in EF processes, leading to the formation of the desired H_2O_2. $4e^-$ ORR represents a parasitic reaction with respect to $2e^-$ ORR, consuming O_2 to directly produce H_2O:

$$O_2 + 2e^- + 2H^+ \rightarrow H_2O_2 \quad \text{(S2)}$$

$$O_2 + 4e^- + 4H^+ \rightarrow H_2O \quad \text{(S3)}$$

S5.2 Degradation tests

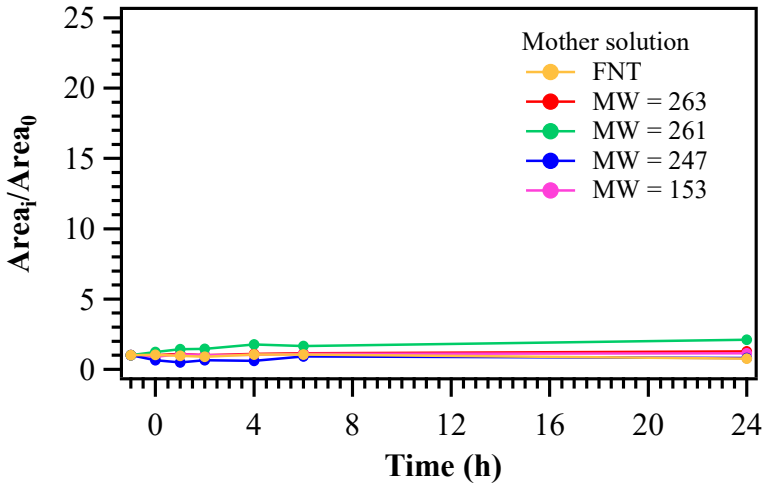

Figure S9. Evolution of FNT and its degradation products during "blank" degradation experiment.

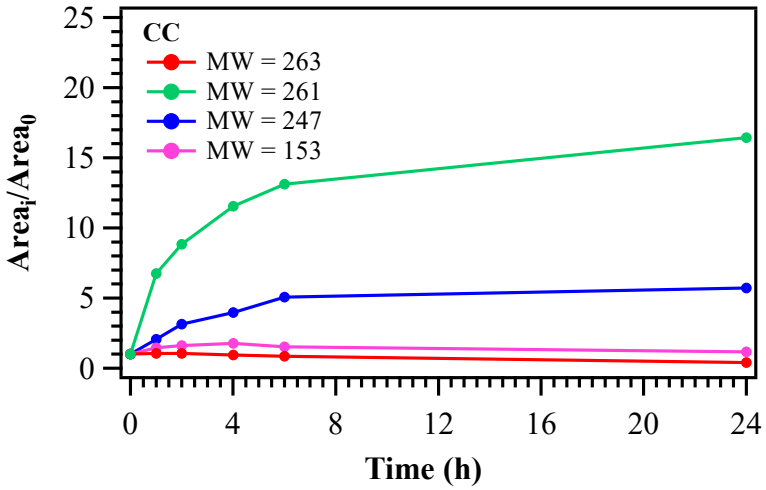

Figure S10. Evolution of FNT-derived degradation products during EF test with bare CC.

S5.3 Analysis after degradation tests

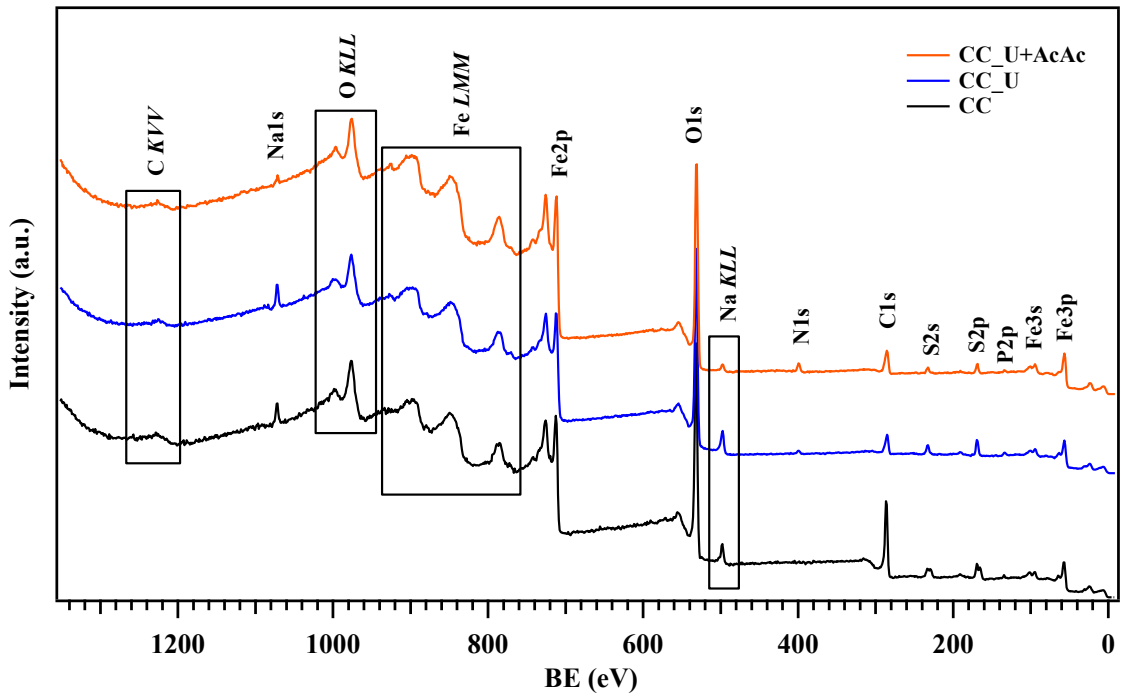

Figure S11. (a) Wide-scan XPS spectra for CC, CC_U and CC_U+AcAc, after EF tests for FNT degradation.

	N_0		N_1		N_2		N_3	
sample	**BE (eV)**	**%**	**BE (eV)**	**%**	**BE (eV)**	**%**	**BE (eV)**	**%**
CC_U	398.9	54.2	400.1	24.9	401.0	13.3	404.8	7.6
CC_U+AcAc	389.9	52.0	400.1	23.2	401.2	18.6	404.8	6.2

Table S7. BE values and percentage contribution of the various components to the overall N1s signal for the investigated specimens, after EF tests. Peak labelling as in Fig. S4b, 2c and 8d-e (main paper).

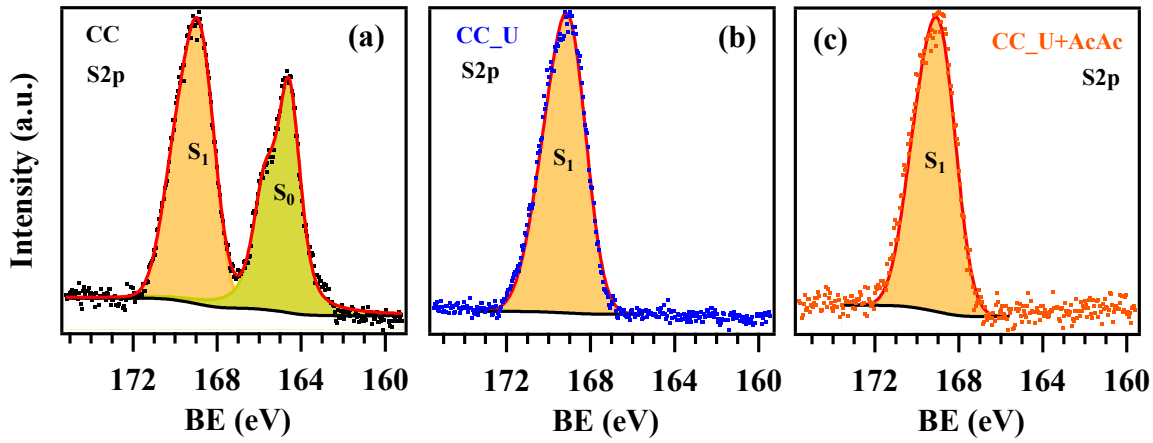

Figure S12. S2p photoelectron peaks for CC (a), CC_U (b) and CC_U+AcAc (c), after EF tests.

As regards sulphur, each band ($\mathbf{S_0}$ and $\mathbf{S_1}$) contains the $2p_{3/2}$ and $2p_{1/2}$ contributions, with a spin-orbit separation of 1.2 eV.[26] The $\mathbf{S_1}$ band, present in all samples, can be related to the presence of sulfate[26] and, in particular, Na_2SO_4,[33] and $Fe_2(SO_4)_3$. In a different way, the $\mathbf{S_0}$ band is associated to the presence of organic sulphides,[26, 27] resulting, in turn, from the presence of FNT and/or FNT decomposition products adsorbed on the sample surface, where the sulphur contained in the S=P-$(OR)_3$ fragment has not been oxidized. This observation suggests that bare CC as cathode displayed an inferior oxidative capability compared to CC_U and CC_U+AcAc, as the specimens with gCN were likely able to completely oxidize to SO_4^{2-} any FNT-derived fragment containing sulphur bonded as sulphide.

	$\mathbf{S_0}$		$\mathbf{S_1}$	
sample	**BE (eV)**	**%**	**BE (eV)**	**%**
CC	164.6	46.3	168.8	53.7
CC_U	-	-	168.8	100
CC_U+AcAc	-	-	168.7	100

Table S8. BE values and percentage contribution of the various components to the overall S2p signal for the investigated specimens, after EF tests. In both cases, the BE values are referred to the $S2p_{3/2}$ spin-orbit split component. Peak labelling as in Fig. S12.

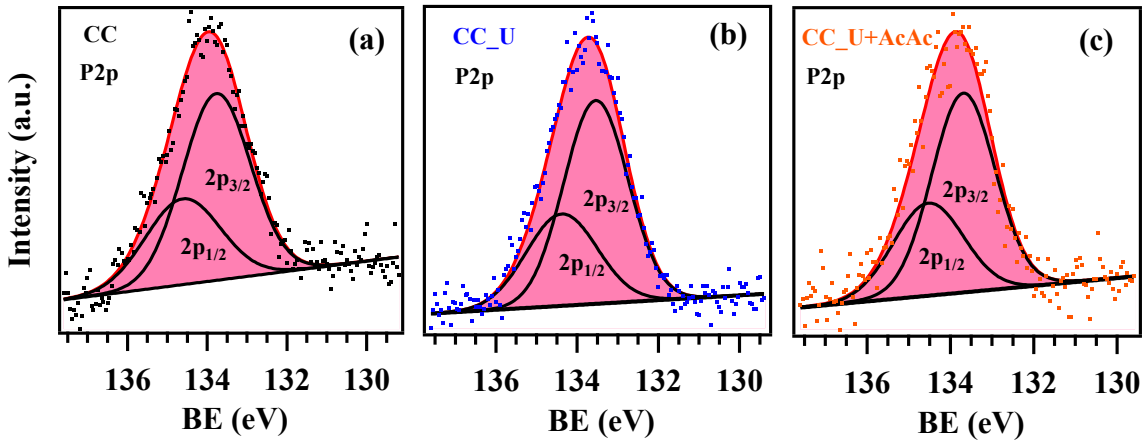

Figure S13. P2p photoelectron peaks for CC (a), CC_U (b) and CC_U+AcAc (c), after EF tests.

For all the three samples, P2p fitting was performed through a deconvolution using the two components $2p_{3/2}$ and $2p_{1/2}$, with a spin-orbit separation of 0.8 eV.[26] The peak position (133.7 eV), corresponding to the $2p_{3/2}$ component, is attributable to the presence of phosphorus (V), bonded as $FePO_4$ on the surface of the samples, presumably derived from PO_4^{3-} moieties, resulting from FNT degradation.[27, 34]

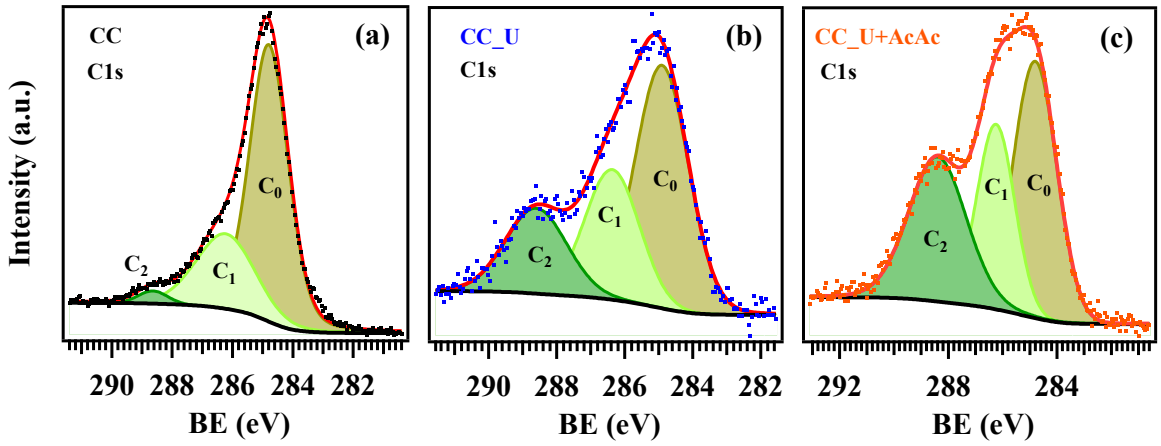

Figure S14. C1s photoelectron peaks for CC (a), CC_U (b) and CC_U+AcAc (c), after EF tests.

In the C1s spectra plotted in Fig. S14, $\mathbf{C_0}$, the most intense band, resulted from both the carbon cloth and adventitious contamination.[26-28] $\mathbf{C_1}$ can be assigned to C-O-C and C-OH moieties,[26, 28] whereas $\mathbf{C_2}$, not present in the as-prepared specimen, can be attributed to carboxylic and/or ester groups.[26, 28] The relative increase in the $\mathbf{C_1}$ component compared to the original systems (compare Tables S3 and S6) and the appearance of the $\mathbf{C_2}$ band indicate the presence of a higher amount of oxidized carbon species. The latter, in the case of CC_U and CC_U+AcAc (see the main paper text), can be ascribed to compounds derived from the partial degradation of FNT, absorbed onto the working electrode.

	$\mathbf{C_0}$		$\mathbf{C_1}$		$\mathbf{C_2}$	
sample	**BE (eV)**	**%**	**BE (eV)**	**%**	**BE (eV)**	**%**
CC	284.8	69.8	286.2	28.0	288.6	2.2
CC_U	284.8	51.8	286.3	27.4	288.5	20.8
CC_U+AcAc	284.8	41.4	286.2	26.0	288.4	32.6

Table S9. BE values and percentage contribution of the various components to the overall C1s signal for the investigated specimens, after EF tests. Peak labelling as in Fig. S4a.

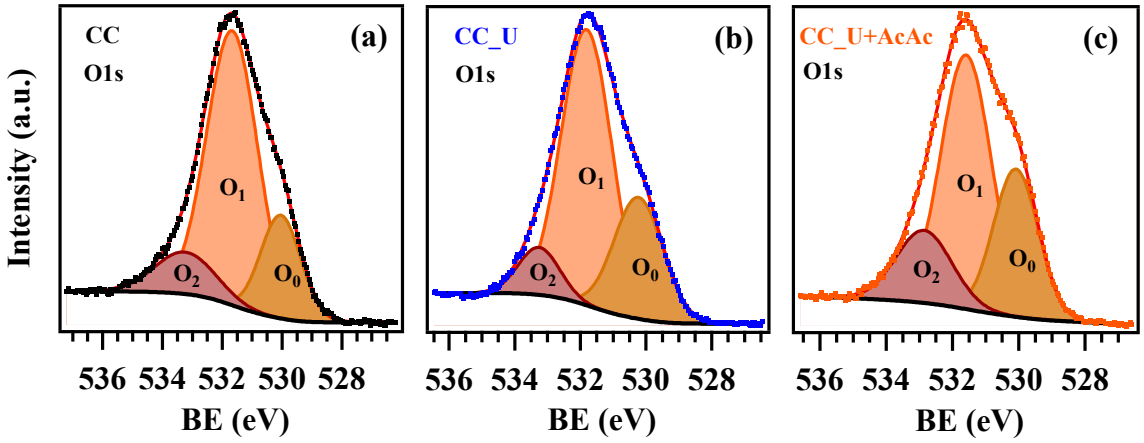

Figure S15. O1s photoelectron peaks for CC (a), CC_U (b) and CC_U+AcAc (c), after EF tests.

O1s peak fitting was performed through a three-band deconvolution. **O_0** band is attributable to oxygen in Fe<u>O</u>OH,[35-39] whereas **O_2** band can be associated with the presence of molecularly adsorbed water and oxygen atoms in carboxylic groups.[28] The origin of latter ones can be traced to the partial oxidation of exposed CC and to the presence of adsorbed FNT-derived fragments, as discussed in the main paper text and ESI (see Fig. S12 and Table S8). The **O_1** band, the most intense in all three cases, encompasses contributions from oxygen atoms in various chemical environments: C-<u>O</u>H,[28] $FeP\underline{O}_4$,[34, 40] $Na_2S\underline{O}_4$ [33] and Fe<u>O</u>OH.[35-39]

	O_0		O_1		O_2	
sample	**BE (eV)**	**%**	**BE (eV)**	**%**	**BE (eV)**	**%**
CC	530.0	19.7	531.6	68.2	533.2	12.1
CC_U	530.2	27.2	531.8	63.8	533.2	9.0
CC_U+AcAc	530.1	28.1	531.6	54.5	532.9	17.4

Table S10. BE values and percentage contribution of the various components to the overall O1s signal for the investigated specimens, after EF tests. Peak labelling as in Fig. S15.

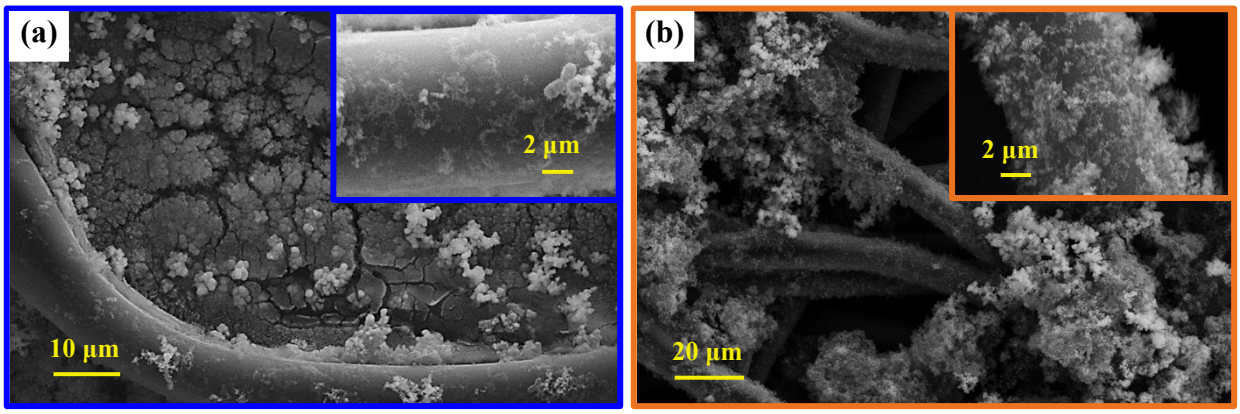

Figure S16. FE-SEM micrographs after EF experiments showed that, whereas for CC_U (a) the deposit completely covers some carbon fibres filling the voids between them, for CC_U+AcAc (b) the deposit features a porous and irregular morphology, leaving empty spaces between the cloth's meshes.

§ S.6. References

1 J. Yang, Z. Ji and S. Zhang, *ACS Appl. Energy Mater.*, 2023, **6**, 3401-3412.

2 S. Zhang, J. Yan, S. Yang, Y. Xu, X. Cai, X. Li, X. Zhang, F. Peng and Y. Fang, *Chin. J. Catal.*, 2017, **38**, 365-371.

3 M. Benedet, A. Gallo, C. Maccato, G. A. Rizzi, D. Barreca, O. I. Lebedev, E. Modin, R. McGlynn, D. Mariotti and A. Gasparotto, *ACS Appl. Mater. Interfaces*, 2023, **15**, 47368-47380.

4 E. Brillas, I. Sirés and M. A. Oturan, *Chem. Rev.*, 2009, **109**, 6570-6631.

5 H. Montigaud, B. Tanguy, G. Demazeau, I. Alves, M. Birot and J. Dunogues, *Diamond Relat. Mater.*, 1999, **8**, 1707-1710.

6 C. Li, C.-B. Cao and H.-S. Zhu, *Mater. Lett.*, 2004, **58**, 1903-1906.

7 J. Yu, K. Wang, W. Xiao and B. Cheng, *Phys. Chem. Chem. Phys.*, 2014, **16**, 11492-11501.

8 J. Liu, T. Zhang, Z. Wang, G. Dawson and W. Chen, *J. Mater. Chem.*, 2011, **21**, 14398.

9 M. Benedet, G. A. Rizzi, A. Gasparotto, O. I. Lebedev, L. Girardi, C. Maccato and D. Barreca, *Chem. Eng. J.*, 2022, **448**, 137645.

10 S. E. Rodil, A. C. Ferrari, J. Robertson and S. Muhl, *Thin Solid Films*, 2002, **420**, 122-131.

11 W. Zhang, Q. Zhang, F. Dong and Z. Zhao, *Int. J. Photoenergy*, 2013, **2013**, 1-9.

12 Y. Zheng, Z. Zhang and C. Li, *J. Photochem. Photobiol., A*, 2017, **332**, 32-44.

13 V. Devthade, D. Kulhari and S. S. Umare, *Mater. Today Proc.*, 2018, **5**, 9203-9210.

14 M. Ismael, Y. Wu, D. H. Taffa, P. Bottke and M. Wark, *New J. Chem.*, 2019, **43**, 6909-6920.

15 S. Benedoue, M. Benedet, A. Gasparotto, N. Gauquelin, A. Orekhov, J. Verbeeck, R. Seraglia, G. Pagot, G. A. Rizzi, V. Balzano, L. Gavioli, V. D. Noto, D. Barreca and C. Maccato, *Nanomaterials*, 2023, **13**, 1035.

16 Y. Yang, G. Zeng, D. Huang, C. Zhang, D. He, C. Zhou, W. Wang, W. Xiong, X. Li, B. Li, W. Dong and Y. Zhou, *Appl. Catal., B*, 2020, **272**, 118970.

17 B. Jurgens, E. Irran, J. Senker, P. Kroll, H. Muller and W. Schnick, *J. Am. Chem. Soc.*, 2003, **125**, 10288-10300.

18 C. Qiu, Y. Xu, X. Fan, D. Xu, R. Tandiana, X. Ling, Y. Jiang, C. Liu, L. Yu, W. Chen and C. Su, *Adv. Sci.*, 2019, **6**, 1801403.

19 Y. Hu, Y. Shim, J. Oh, S. Park, S. Park and Y. Ishii, *Chem. Mater.*, 2017, **29**, 5080-5089.

20 L. Florentino-Madiedo, E. Díaz-Faes and C. Barriocanal, *Carbon*, 2022, **187**, 462-476.

21 P. Zhang, Y. Tong, Y. Liu, J. J. M. Vequizo, H. Sun, C. Yang, A. Yamakata, F. Fan, W. Lin, X. Wang and W. Choi, *Angew. Chem. Int. Ed.*, 2020, **59**, 16209-16217.

22 Y.-X. Ye, C. Wen, J. Pan, J.-W. Wang, Y.-J. Tong, S. Wei, Z. Ke, L. Jiang, F. Zhu, N. Zhou, M. Zhou, J. Xu and G. Ouyang, *Appl. Catal., B*, 2021, **285**, 119726.

23 M. Benedet, G. A. Rizzi, D. Barreca, A. Gasparotto and C. Maccato, *Surf. Sci. Spectra*, 2023, **30**, 014004.

24 Y. Wang, H. Wang, F. Chen, F. Cao, X. Zhao, S. Meng and Y. Cui, *Appl. Catal., B*, 2017, **206**, 417-425.

25 Y. Chen, X. Liu, L. Hou, X. Guo, R. Fu and J. Sun, *Chem. Eng. J.*, 2020, **383**, 123132.

26 J. F. Moulder, W. F. Stickle, P. E. Sobol and K. D. Bomben, *Handbook of X-ray Photoelectron Spectroscopy*, Perkin Elmer Corporation, Eden Prairie, MN, USA, 1992.

27 https://srdata.nist.gov/xps, accessed October, 2023.

28 I. Bertóti, M. Mohai and K. László, *Carbon*, 2015, **84**, 185-196.

29 J. Zhu, L. Kong, X. Shen, G. Zhu, Z. Ji, K. Xu, H. Zhou, X. Yue and B. Li, *J. Electroanal. Chem.*, 2020, **873**, 114390.

30 S. Fukuzumi, Y. Yamada and K. D. Karlin, *Electrochim. Acta*, 2012, **82**, 493-511.

31 Y. Yamada, Y. Fukunishi, S. Yamazaki and S. Fukuzumi, *Chem. Commun.*, 2010, **46**, 7334-7336.

32 J.-y. Chen, N. Li and L. Zhao, *J. Power Sources*, 2014, **254**, 316-322.

33 M. Wahlqvist and A. Shchukarev, *J. Electron. Spectrosc. Relat. Phenom.*, 2007, **156-158**, 310-314.

34 Y. Liu, Z. Li, Y. You, X. Zheng and J. Wen, *RSC Adv.*, 2017, **7**, 51281-51289.

35 L. Yang, Y. Liu, J. Li and G. Du, *J. Alloys Compd.*, 2018, **763**, 134-140.

36 I. D. Welsh and P. M. Sherwood, *Phys. Rev. B: Condens. Matter*, 1989, **40**, 6386-6392.

37 J. Liu, M. Zheng, X. Shi, H. Zeng and H. Xia, *Adv. Funct. Mater.*, 2015, **26**, 919-930.

38 A. N. Mansour and R. A. Brizzolara, *Surf. Sci. Spectra*, 1996, **4**, 357-362.

39 Y. Sun, X. Hu, W. Luo, H. Xu, C. Hu and Y. Huang, *ACS Appl. Mater. Interfaces*, 2013, **5**, 10145-10150.

40 Y. Wang and P. M. A. Sherwood, *Surf. Sci. Spectra*, 2002, **9**, 99-105.